UU-NF 01#09 (December **2001)**
Uppsala University Neutron Physics Report

ISSN 1401-6269

Editor: Jan Källne

NEUTRON EMISSIVITY PROFILE CAMERA DIAGNOSTICS CONSIDERING PRESENT AND FUTURE TOKAMAKS

SIMON FORSBERG

UU-NF 01#09 (**December 2001**)
Uppsala University Neutron Physics Report

ISSN 1401-6269

Editor: Jan Källne

NEUTRON EMISSIVITY PROFILE CAMERA DIAGNOSTICS CONSIDERING PRESENT AND FUTURE TOKAMAKS

Simon Forsberg

Department of Neutron Research
Ångström Laboratory
Uppsala University
Box 525
S-751 20 UPPSALA, Sweden

Abstract

This thesis describes the neutron profile camera situated at JET. The profile camera is one of the most important neutron emission diagnostic devices operating at JET. It gives useful information of the total neutron yield rate but also about the neutron emissivity distribution. Data analysis was performed in order to compare three different calibration methods. The data was collected from the deuterium campaign, C4, in the beginning of 2001. The thesis also includes a section about the implication of a neutron profile camera for ITER, where the issue regarding interface difficulties are in focus. The ITER JCT (Joint Central Team) proposal of a neutron camera for ITER is studied in some detail.

Contents

1 Introduction

The energy that originates from the sun and other stars in the universe is due to thermonuclear reactions through fusion of light nuclides. Thermonuclear fusion can release a large amount of energy as it is due to the difference in binding energies per nucleon of the reacting and produced nuclides. If two nuclides with relatively low binding energies are fused into one of higher binding energy, E_b, the difference will, in most cases, be released as kinetic energy carried by the particles produced; in some rare cases the energy release will come as γ-radiation. Kinetic energy is easily transformable to other forms of energy and has therefore great utility value. The thermonuclear phenomenon has a great potential to become the source that will secure the future energy supply.

1.1 Fusion fuels and reactions

It is only possible to produce energy through fusion of particles with a mass number, A, less than 56. For A larger than 56, it is possible to produce energy through

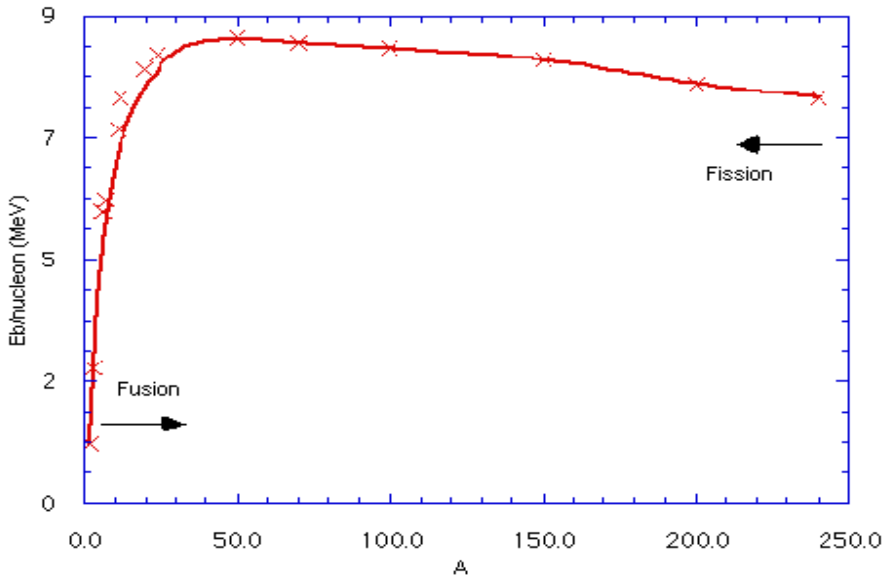

Fig. 1.1: The binding energy per nucleon. Illustrates when energy release originates from fusion and fission respectively.

fission. Figure 1.1 shows the binding energy per nucleon for different nuclides. An important distinction between fusion and fission is that the energy release through fusion is due to thermal reactions whilst the fission process is a chain of neutron induced reactions. To get two particles to fuse one must overcome the Coulomb barrier. This barrier increases with nuclear charge (Z) and therefore different isotopes of hydrogen, with Z=1, are preferable fusion fuels. Four of the most common fusion reactions give energy release in the range 3 to 18 MeV. They are

$$D + D \rightarrow n + {}^{3}He + 3.3MeV \quad (1.1)$$

$$D + D \rightarrow p + T + 4.0MeV \quad (1.2)$$

$$D + T \rightarrow n + {}^{4}He + 17.6MeV \quad (1.3)$$

$$D + {}^{3}He \rightarrow p + {}^{4}He + 18.3MeV \quad (1.4)$$

The first two reactions have approximately the same probability to occur. In a future thermonuclear reactor, D and D-T plasmas are considered to be the most suitable ones. The D plasma is attractive because deuterium is a stable isotope and exists naturally in seawater; about 0.015% of the hydrogen in water is deuterium. D-T fuel is considered because of its large D-T cross section. Moreover, the energy release is large, 17.6 MeV, of which the neutron carries 14.1 MeV while the remaining 3.5 MeV is carried by the α-particle. The drawback is that tritium is unstable with a half-life of 12 years. It does not exist naturally (except for short periods) and consequently has to be produced in some way. One way is to breed tritium through neutron bombardment of lithium. The tritium breeding reactions in lithium, of which there are two isotopes existing naturally, ^{6}Li (7.5%) and ^{7}Li (92.5%), are

$$n + {}^{6}Li \rightarrow T + {}^{4}He \quad (1.5)$$

$$n + {}^{7}Li \rightarrow {}^{6}Li + 2n \quad (1.6)$$

Reaction (1.5) is exothermic and releases 4.9 MeV while reaction (1.6) is endothermic and calls for an input energy of E_n=7.2 MeV; the neutrons come from reaction (1.3) having kinetic energies up to 14 MeV. The lithium supply in earth's crust is estimated to be about of the same order of magnitude as the world's available fossil resources [1]. The oceans, however, are a practically inexhaustible source of lithium.

To burn, the fusion fuel is heated to a level where the atoms lose their electrons and become ionized; i.e., the atomic gas gets converted into an ionized gas forming a *plasma* which is the fourth state of matter. Plasmas have the advantage that they can be confined to limited volume by magnetic fields, configured so that they act as magnetic bottles. In fusion research this property is of fundamental importance.

1.2 The JET tokamak

Tokamak is an acronym for Toroidalnya Kamera and Magnitnaya Katushka, which is Russian and means toroidal chamber and magnetic coils. The largest tokamak today is the JET (Joint European Torus) machine, situated at Culham science center, Oxfordshire, UK. The tokamak has been operated since 1983 and it took four

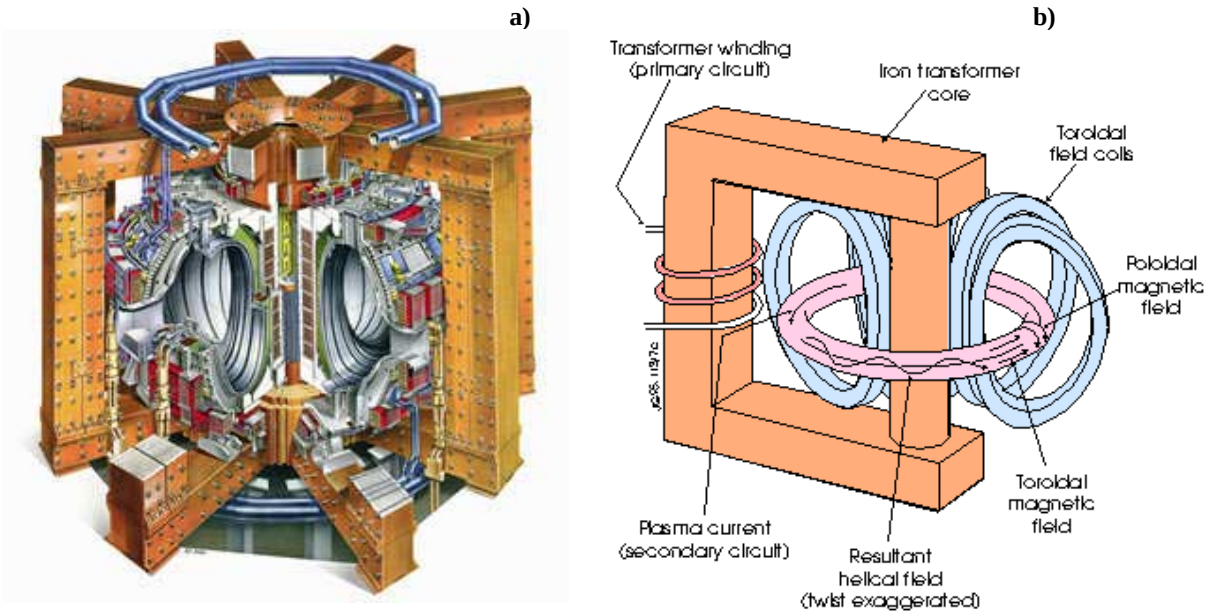

Fig. 1.2: a) A schematic of the JET facility showing the D-shaped cross-section and the transformer iron core. b) Showing the poloidal field coils and the toroidal plasma current that together results in a helical field. It is also shown that the plasma itself acts as secondary circuit in the transformer.

years to build it [2]. The JET Joint Undertaking was established in 1978 to construct and operate the device but since 2000, EFDA (European Fusion Development Agreement) and UKAEA (United Kingdom Atomic Energy Authority) carry out the management and operation of JET [3].

The poloidal cross section of the JET torus is D-shaped with a plasma height-width ratio (elongation) of typically 1.6. The total device height is 11.5 m and the overall diameter is 14.8 m (figure 1.2 a). The plasma is confined inside the tokamak through poloidal and toroidal magnetic fields. The poloidal field is due to the toroidal plasma current, which is induced by the primary circuit of the transformer. The toroidal field is produced with 32 poloidal coils that surround the tokamak. As illustrated in figure 1.2 b, these two crossed fields form helical magnetic field lines. These field lines are closed in the whole vessel except for the lines just inside the vessel wall, which can have a x-point at the bottom, and sometimes at the top as well. The gross motion of the plasma particles follow these field lines, so charged particles escape only at the trajectories defined of the x-point. In this case they end up in the so-called divertor. To avoid impurities to enter the vessel (toroidal chamber) it was built to hold a vacuum better than 10^{-3} torr [2].

1.3 Heating the plasma

Except for the ohmic heating due to the plasma current (≤ 7 MA) there are three major techniques available at JET to heat the confined plasma. The first is based on neutral beam (NB) injection. Here positive ions are accelerated by an electric field created from a high voltage source (~ 140 kV) and formed into a beam which is neutralized when passing through a gas cell. The neutral beam can pass the magnetic field of the tokamak and penetrate into the plasma where the beam atoms become ionized and lose their energy through Coulomb collisions. Today the maximum NB power available with is $P_{NB} \approx 21$ MW.

The second method uses electromagnetic waves of a frequency that resonates with the plasma and thus causing heating. When the ions starts to resonate they get accelerated and consequently absorb energy. The radio frequency (RF) waves are emitted from

antennas situated on the walls inside the vessel ($P_{RF} \leq 20$ MW at JET). This method is called ICRH (Ion Cyclotron Resonance Heating) or simply RF heating.

A related technique is LHCD (Lower Hybrid Current Drive). In short this means that microwaves at frequencies between the electron and ion cyclotron frequencies are applied in order to accelerate the plasma electrons. This is mostly used to increase the plasma current but can also be used for heating the plasma.

Another heating method may be added to JET during the EP-program (Enhanced Performance) to start 2003. The method will be equivalent to ICRH but instead of applying electromagnetic waves to the plasma ions the electrons now are the targets. This method is logically named Electron Cyclotron Resonance Heating (ECRH). The aim is to be able to contribute up to 5 MW of heating power.

In contemporary fusion research, one of the main goals is to create self-heating conditions in order to maintain the plasma temperature at a sufficiently high level ($>10^7$ ^oC). In such a regime, the plasma is said to ignite. This can be achieved if the α-particles (carrying 3.5 MeV kinetic energy) produced by reaction (1.3) above give up a sufficiently large amount of energy before escaping the plasma. Ignition is still a target to be realized calling for further research. Theories in this field of study may be put into practice when the next generation of tokamaks becomes reality.

1.4 ITER - the next step

The next large-scale fusion device, ITER (International Thermonuclear Experimental Reactor), is now in the final design stage. With this tokamak the aim is to raise the fusion power production level several orders of magnitude compared to present tokamaks and enabling the study of burning plasmas. The plasma size of ITER approximately twice of that of JET, the largest tokamak existing today, and the plasma volume will increase more than eight times from about 100 m^3 to fully 800 m^3 [4].

ITER is a collaboration project between the Euroatom, Japan and Russia. Originally the USA was also involved but they decided to abandon the project in 1999.

1.5 Neutron diagnostics

The number of diagnostic systems at JET has increased steadily since its operational beginning, when only 28 diagnostics systems were in use. In 1998, the peak was reached with 70 different diagnostics [5]. Most of the diagnostic devices are mounted on the tokamak and "look" into the plasma through ports in the vessel wall.

Neutron diagnostics play an important role in contemporary fusion research and will do so even more in the future. Measuring the neutron emission gives fundamental information about the plasma, such as on the fusion reactivity and the fuel ion state (e.g., temperatures, densities, etc). There are three primary types of neutron measurements involved. Fission chambers, containing ^{238}U and ^{235}U, are employed to measure the average neutron flux from the plasma and are calibrated to give the total neutron yield rate (Y_n) and hence the reactivity; these are referred to as the KN1 diagnostics at JET. To gain detailed information about the fuel ions, a number of neutron spectrometers are used. The detection techniques vary but common to all methods is that one has to let the neutrons interact with a passive or active (e.g. scintillator) target before detection is possible. The interaction most commonly used is nuclear elastic scattering with protons. The relationship between the energy of the recoil proton produced and the incoming neutron is

$$E_n = E_p(\cos^2\theta)^{-1} \qquad (1.7)$$

where θ is the proton scattering angle.

The charged particles produced (i.e., protons in this case) have the ability to excite the scintillator molecules which, in turn, emits characteristic light in the scintillator that can be detected. The time-of-flight spectrometer, for example, measures the time difference between two such events caused by neutrons passing two scintillators, one after the other. This information together with the known geometry makes it possible to derive the energy of the incident neutrons.

Another spectrometer is based on the MPR (magnetic proton recoil) technique. Here the scattered protons are momentum analyzed through their bent trajectories in an magnetic field, ending at a position sensitive detector (hodoscope). Detailed response functions are used to derive the neutron energy spectrum from the proton distribution

over the hodoscope. The FWHM (full width half maximum) of the neutron spectrum is proportional to the square root of the plasma temperature [6].

Different NES (neutron emission spectroscopy) techniques result in different experimental capabilities such as, energy resolution and detection efficiency. Choosing the most appropriate technique is first of all based on the required balance between these two parameters. Of course, cost is a matter that has to be considered as well, besides other important performance parameters for the NES applications at hand.

The third kind of neutron diagnostics is concerned with measurement of the neutron flux received by linear collimator arrays (cameras) whose sight lines intersect the poloidal cross section of the plasma. With two orthogonal (horizontal and vertical) neutron cameras, one can acquire data from which one can, in principle, re-construct the neutron emissivity of the plasma over the poloidal plane.

1.6 JET Data

The raw data produced after each plasma pulse is stored in JPF's (Jet Pulse Files). These files are stored in the JET Solaris Unix-system within a few minutes after a pulse. To convert the diagnostic data into useful information the, JPF's have to be processed. For many diagnostics, this process is run automatically after each pulse by Intershot Analysis routines and the results are stored in PPF's (Processed Pulse Files). For some cases, PPF production is performed manually by analysis programs such as YAPAN, which will be discussed later in this thesis.

The overall data supervision at JET is handled by CODAS (COntrol and Data Acquisition System).

1.7 Present study

This thesis will mostly be concerned with the JET neutron emission profile monitor (camera) and its use as a plasma diagnostic. The work has been carried out partly at JET, Oxfordshire, UK, and partly at the Department of Neutron Research (INF) in Uppsala, Sweden. The thesis contains data analysis parts as well as more informative parts based on available literature. The diagnostic system is described in section 2.1. A

principal part of the present work is about the calibration of the camera detectors. The calibration system and procedures are presented in section2.2-2.3 as well as the detailed interpretation of related data. In order to compare three different kinds of calibration methods, an analysis of calibration data acquired at JET was performed (chapter 3). The issue about drifts in the discriminator threshold is also considered (chapter 4). Here a qualitative estimation was made to evaluate what consequences a threshold drift could cause. The neutron camera diagnostic system is discussed in chapter 5, in particular, from the perspective of implications on ITER. The conclusions of this report are presented in chapter 6.

2 The JET neutron emission profile monitor

The JET neutron profile monitor (referred to as the KN3 diagnostic at JET) has several functions. Its main task is to measure the 2.5-MeV neutron flux spatial distribution from D plasmas, originating from the $D + D \rightarrow {}^3He + n$ reaction. This system was first installed at JET in September 1986 and later (August 1987) improved. Further upgrading was done in the middle of the nineties, which included added capability for measuring 14-MeV neutrons originating from the $D + T \rightarrow \alpha + n$ reaction in D-T plasmas.

Information about how the plasma neutron emission varies with time during a discharge can be gained through recording time traces of neutron flux for each channel of the cameras. By summing the count rates in all channels, the total neutron yield rate (Y_n) can be determined; by summing also over time, the total neutron yield of a discharge can be determined. Together, the vertical and horizontal cameras provide a data set of nineteen line-integrated neutron emissivities. From these data, neutron emissivity profiles can be obtained with the analysis program, YAPAN. Neutron profiles give information about the spatial plasma position. Moreover, they also contain detailed shape information that shows various magnetohydrodynamic (MHD) effects occurring during the plasma discharge.

2.1 System design

The profile monitor consists of a pair of neutron collimator arrays (cameras). As shown in figure 2.1 one is situated above the tokamak in the torus hall (vertical camera) and the other one to the side (horizontal camera). The horizontal camera has ten lines-of-sight (channels nos. 1-10) while the vertical one has nine (nos. 11-19). Each channel consists of a collimator and a detector assembly with local shielding. The collimator cross sections are rectangular measuring 44 x 25 mm^2 (horizontal camera), and vary from 25 x 18 mm^2 (channel 11) to 25 x 25 mm^2 (channel 19) for the vertical camera. Collimator inserts make it possible to reduce the aperture. The collimator arrays are placed in blocks made of high density concrete. These assemblies together with the detectors constitute the cameras. The detectors require shielding against background radiation of γ-rays and scattered neutrons, which is most provided by the concrete.

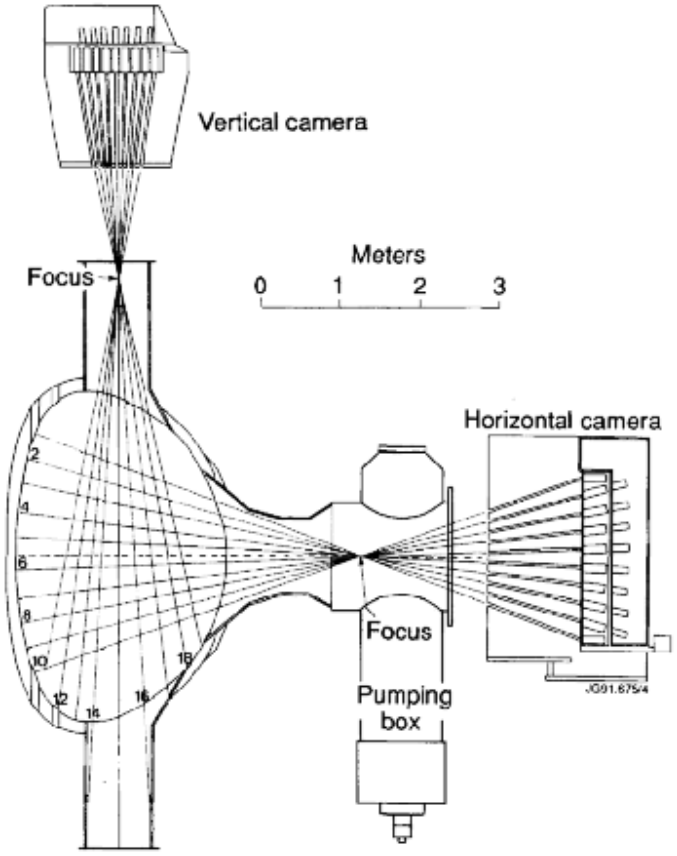

Fig. 2.1: Schematic of the JET neutron profile monitor, showing the 19 lines-of-sight. Channel 1-10 represents the horizontal camera and channel 11-19 represents the vertical camera.

The camera detectors are of two types based on liquid scintillators (NE-213, of diameter ∅=2.5 cm) and plastic scintillators (Bicron BC-418, ∅=1.5 cm). These 1-cm thick scintillators are coupled to photomultiplier (PM) tubes (Thorn-EMI 9815). The PM-tubes are enclosed in a magnetic shielding of 3-layered cylinders of materials with varying (outward decreasing) permeability.

The NE-213 scintillator detectors have been used since the beginning of KN3. The Bicron plastic scintillator detectors, on the other hand, were not installed until 1997, just in time for the DTE1 (Deuterium-Tritium Experiment 1) campaign [7]. The plastic scintillators are used to detect 14-MeV neutrons from D-T plasmas [8]. The liquid scintillators are used to measure the 2.5-MeV neutron flux from D plasmas since these have the essential capability of separating γ-ray induced events from the signal events due to the neutrons. The separation is carried out by pulse shape discrimination (PSD) which can be done as γ-pulses are of shorter duration than those of neutrons are. By using two sets of PSD modules it becomes possible to distinguish also between 2.5-MeV and 14-MeV neutrons.

The absolute neutron detection efficiency for 2.5-MeV neutrons has been determined to ~$2.4*10^{-2}$ per neutrons/cm^2 [9] and vary up to 10 % [10].

2.2 Experimental data and corrections

Corrections must be applied to the raw data collected by KN3, taking into account channel-to-channel differences including change over time. Most of these originate from the geometry of the system setup or the electronics. Effects to consider are: dead-time, neutron detection efficiency, collimator geometry, neutron scattering and cross-talk between adjacent channels [9].

When two subsequent events occur so close to each other that they cannot be distinguished as two separate ones, they are said to fall within the experimental dead-time. The dead-time can be determined by measuring the output from a signal source with well known frequency. Determination of the dead-time in KN3 was done by measuring the fluctuations from a 2-MHz oscillator. Correcting for the dead-time effect is essential when the count rate is high.

For a plasma neutron to reach the camera detector it must pass through a port window as well as the detector housing which causes some flux attenuation. Moreover, not all detected neutrons come directly from the plasma as some could have. Before reaching the scintillator, some neutrons scatter in the collimator wall or the plasma vessel (in- and back-scattering). To estimate the effects of attenuation and in-scattering, for each camera channel a general Monte Carlo code for neutron and photon transport (MCNP) was used. MCNP is a FORTRAN program developed at Los Alamos National Laboratory for calculations of neutron transport in matter. By specifying the source and the geometry as well as nuclide composition of the structures surrounding it, corrections can be calculated. From calculations of this kind, correction factors were determined to be about 9 % and 17.5 % for the horizontal and vertical cameras, respectively [9].

The effect due to back-scattered neutrons must also be corrected for. This is done by another FORTRAN program called FURNACE. FURNACE permits neutronic (and photonic) calculations in 3D toroidal geometry. The contribution from back-scattered neutrons is low for the central channels but is significant for the peripheral channels where it often can be dominant. The intensity from back-scattered neutrons is approximately constant over the entire vessel. For this reason the back-scattered fraction increases as one moves towards the plasma periphery.

Cross-talk arises when neutrons in one channel are scattered into an adjacent channel to be detected by the "wrong" detector. Measurements have shown that the cross-talk contribution in KN3 is negligible.

2.3 Calibration and γ-discrimination

Because of the linearity between energy and scintillation light output for electrons [11], γ-sources of different kinds can be used for energy calibration of detectors. At JET, radio sources of ^{22}Na are built into the camera detector channels. This source has a half-life of 2.6 years determined by ^{22}Na decay to ^{22}Ne through β^+-emission (90 %) and electron capture (10 %). ^{22}Ne then de-excites through 1274-keV γ-ray emission. When the β^+ interact with matter, 511-keV annihilation γ-ray pairs are produced ($e^+ + e^- \rightarrow 2\gamma$).

The PSD's have four discriminator settings referred to as, *Threshold* (T), *Pile-up* (P), *Lower* (L) and *Upper* (U). The T setting determines the minimum pulse height level for accepted events. The P setting defines the level for rejection of events caused by Pile-up effects which are related to dead-time effects discussed earlier (see section 2.2). They occur at high count rates and involves the superposition of two pulses [11]. The L setting is the discriminator level for selecting 2.5-MeV neutron signal events whilst the U level is used to select neutrons of higher energies, i.e., those from DT-reactions [9].

The first step in the calibration process is to record a γ-ray pulse height spectrum, using the ^{22}Na sources, with the PSD's set to collect all events above the T level. An example of such a pulse height spectrum is shown in figure 2.2.

Since organic scintillators consist mostly of low-Z elements (hydrogen and carbon), γ-rays in the MeV-range interact predominantly through Compton scattering [12]; the photoelectric effect, on the other hand, is weak. In lieu of wanted photopeaks in the γ-ray spectrum, Compton scattering edges must be used of which two can be distinguished in the measured spectrum. The Compton edge energy, E_C, is the maximum kinetic energy transferred to electrons by incident photons of energy E_γ in 180-degree scattering, i.e.,

$$E_C = \frac{2E_\gamma^2}{mc^2 + 2E_\gamma}. \qquad (2.1)$$

The pulse height scale of the recorded γ-ray spectrum can now be expressed in units of electron energy equivalent (i.e., MeV_{ee}).

For heavy charged particles it takes several MeV of energy to produce the same amount of light as for electrons. The reason is that the light emitting de-excitation modes in the scintillator are not strong enough to exhaust the deposited energy because of the high ionization density (quenching, see ref. [11]). The expression used to determine the relationship between pulse height (light output L) and deposited particle kinetic energy (E) is [9]

$$L_p(E_p) = -0.131 + 0.25E_p + 0.03915E_p^2 \qquad (2.2)$$

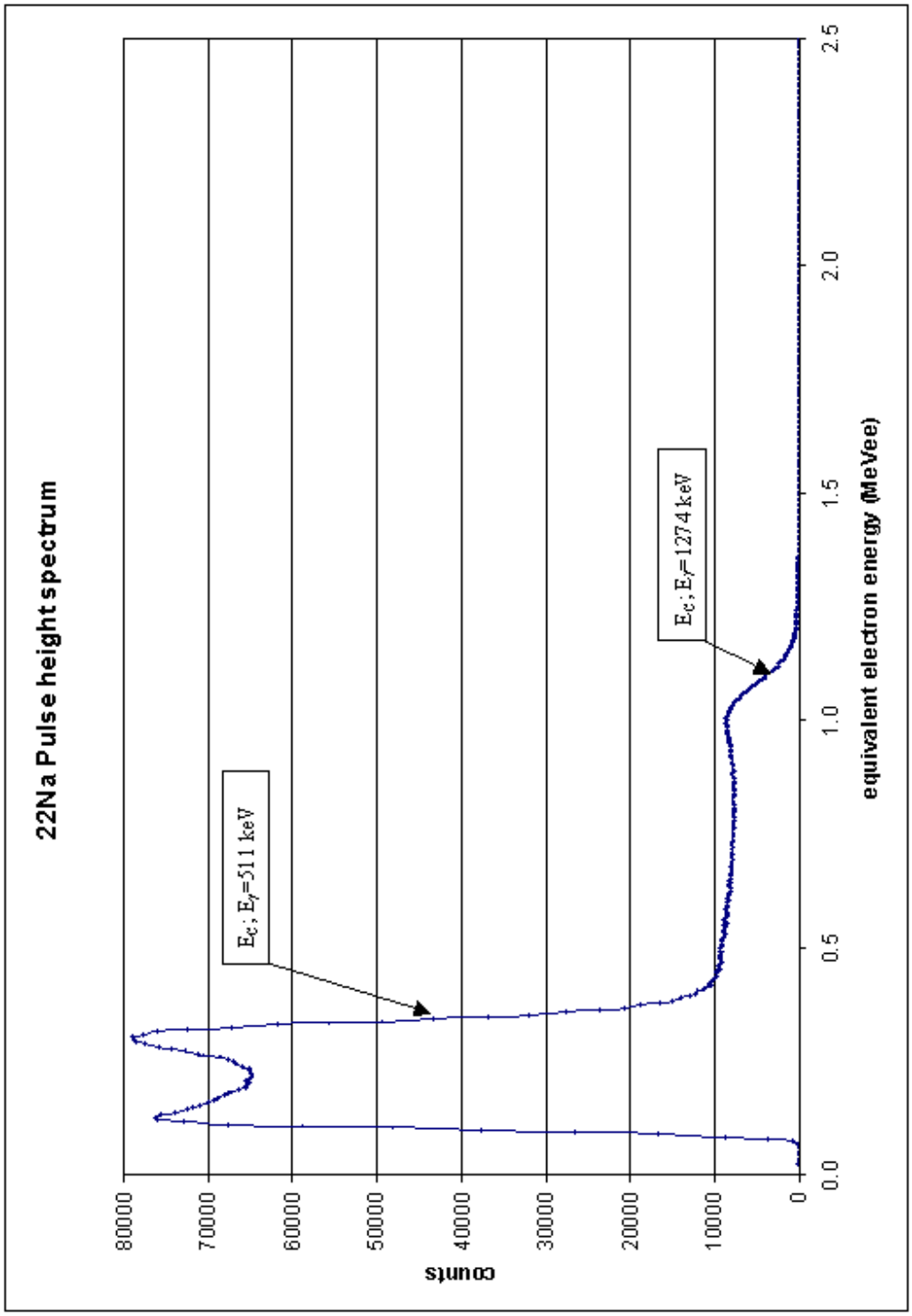

Fig. 2.2: Pulse shape spectrum from a ^{22}Na γ-source. Showing the two Compton edges that arises due to 51- keV and 1274-keV γ-radiation. The x-axis is related to the recoil proton energy in equivalent electron energy (MeVee).

here, L_p is the equivalent electron energy and E_p is the maximum recoil proton energy (assumed to be in the range $1.5 \leq E_p \leq 3.3\,\mathrm{MeV}$).

A special feature of organic scintillators, especially liquid ones such as NE-213, is that the light pulse shape is specific for the ionizing particle; this means that heavy and high-Z particles produce pulses with long decay time [11]. This feature is very useful when one wants to discriminate γ-induced electron events from neutron-induced proton events in the scintillators. This makes it possible to distinguish between the two kinds of events based on pulse shape.

Detailed reference spectra for each channel together with the criterion that the number of γ-events above the discriminator is large enough to minimize the statistical error, enables one to perform a good estimation of the discriminator's cut-off position in the pulse height spectrum. Hence, the stability of the discriminator can be monitored, or more correctly, the combination of the discriminator and PM-tube gain stability. Drifts in this stability affect the extraction of results from the data. It is taken into account by use of a correction factor that is applied to the data after the measurement; no active stabilization of the diagnostic is attempted.

Good statistics is essential for the success of the γ-calibration of the camera detectors. Initially, a method (A) was used. It was based on counting during forty seconds before a plasma, namely, in the period between the countdown start time and the plasma breakdown time. However, as the γ-source weakens over time the calibration routine had to be changed, in order to lengthen the data collection time to maintain good statistics. This was first done by adding up data from discharges during an entire day and then take the average (method B). This improves the calibration accuracy but is unfortunately dependent on the daily fluctuations that can occur when running the tokamak. To avoid this dependency, yet another method (C) was used that utilizes the idle time, of several minutes, between two shots. This gives as good statistics as method B but without the dependency of the daily variations and is the method used today. A comparison of the three methods was done as part of this study.

3. Neutron monitor calibration data and analysis

The calibration data considered in this study relate to approximately a hundred shots selected from the interval of JET pulses with numbers between #53270 and #53570. Only shots with a total neutron yield of more than 10^{14} were chosen. A program called YAPAN (Yet Another Program Analyzing N3) is used to process the raw data in the JPF's of which the results are stored in PPF's; the program is restricted to accept only those discharges with a total neutron yield of larger than ~10^{13}. The same shots were run in YAPAN for the three calibration cases.

The fitting function, reproducing the radial neutron emissivity distribution, used by YAPAN is given by [13]

$$S(\rho) = (S_0 - S_a)(1-\rho^2)^{\alpha} + S_a\,; \qquad (3.1)$$

here, ρ is the normalized minor plasma radius, α is the peaking factor, S_0 is the peak

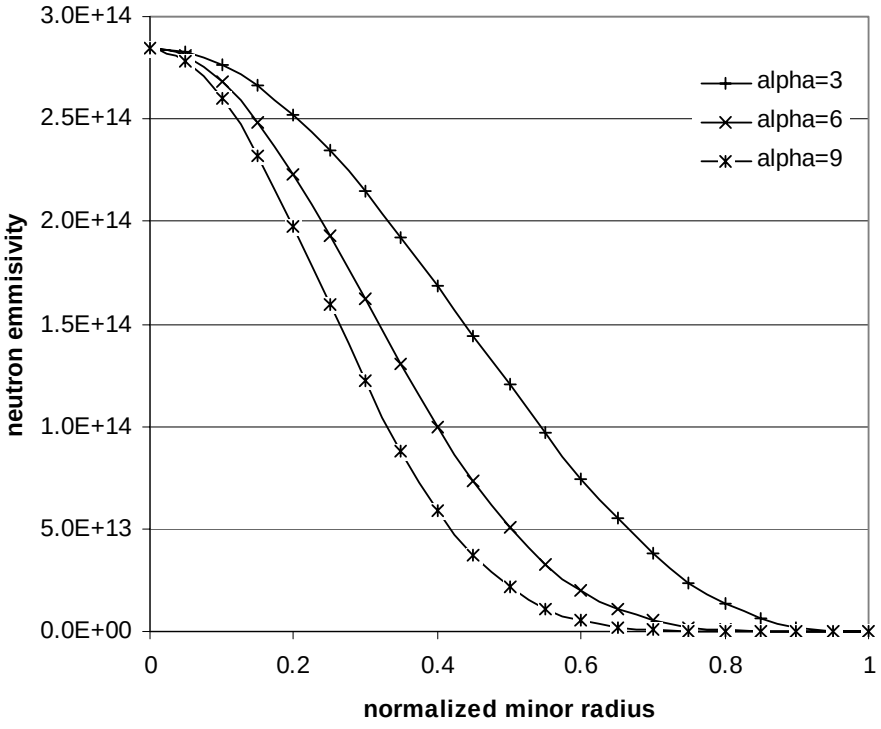

Fig. 3.1: Neutron emissivity functions with peaking factors of α = 3, 6 and 9.

emissivity and S_a is the pedestal. The function has a quasi-parabolic shape where the α parameter determines the peak width so that $1/\alpha^2$ is proportional to the FWHM-value of the curve. Three curves related to different α-values, with the S_0- and S_a-values chosen to be $S_0=2.85*10^{14}$ and $S_a=100$, are shown in figure 3.1.

A FORTRAN code [14] was used to extract relevant data from the PPF's and to convert it into three text files, for which the calibration methods A, B and C were applied. The files contained the following columns: *Shot number*, *Peaking factor*, *Pedestal*, *KN3/KN1 ratio*, χ^2, *Peak emissivity*, *Channel 1-19 response* and *Time*. KN3/KN1 is the ratio between the total neutron yield recorded from KN3 and KN1 (fission chambers) respectively. χ^2 is the fitting parameter which is related to how successful the actual fitting turned out to be. While perfect fitting would give χ^2 values close to one, typical values in the present study are χ^2 between 2 and 15.

The data extracted were time-resolved (approximately 100 bins 50 ms long for each shot) as well as time-integrated data over the entire shot. These two data sets were analyzed separately.

The aim of this analysis is to arrange the data in such way that it is possible to explore which of the calibration methods is most accurate. Basically, there are three major error sources in the data. The principal one has its origin in the neutron yield. The neutron emissivity profile and the statistics of the γ-ray calibration are the two remaining sources that have to be considered. One wants to eliminate those errors that are not due to the calibration procedure, which is the essential issue of the analysis.

3.1 Time resolved data

The data were sorted by time and were combined into new files with rows, now matched by time; times with missing data were excluded. The time matching guarantees that the considered neutron camera channel fluxes are exactly the same for all three cases. This is an important aspect as one wishes to eliminate all error contributions that are not related to the actual calibration procedure.

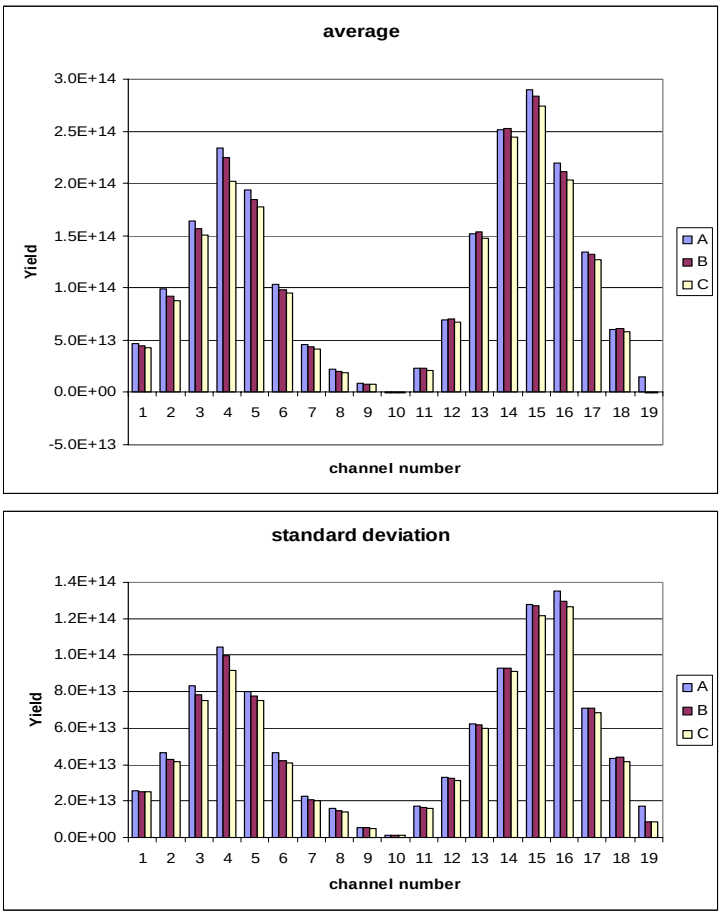

Fig. 3.2: The average neutron yield and standard deviation recorded in channel 1 to 19. The data are time-resolved and collected from approximately a hundred shots within the range #53270 to #53570.

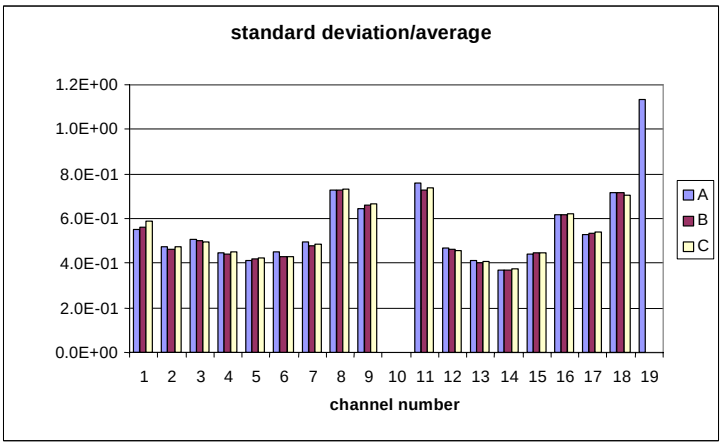

Fig. 3.3: Standard deviation divided with the average value for channel 1 to 19. The negative values for channels 10 and 19 are not shown.

The averages and the standard deviations, of the channel neutron responses, were derived next. This gave the results presented in figure 3.2. The average graph tells us that the neutron yield is larger in the center channels in comparison to the outer ones. This is what one would expect, as the neutron production is concentrated to the plasma core. Channel 10 and 19 returns some small negative average values. This is due to background over corrections made by the KN3 correction software. The standard deviation graph looks similar to the average graph. The conclusion that can be stated from this fact is that the neutron yield varies a lot, both within a discharge but also from discharge to discharge. If this disturbance could be eliminated a much flatter shape would

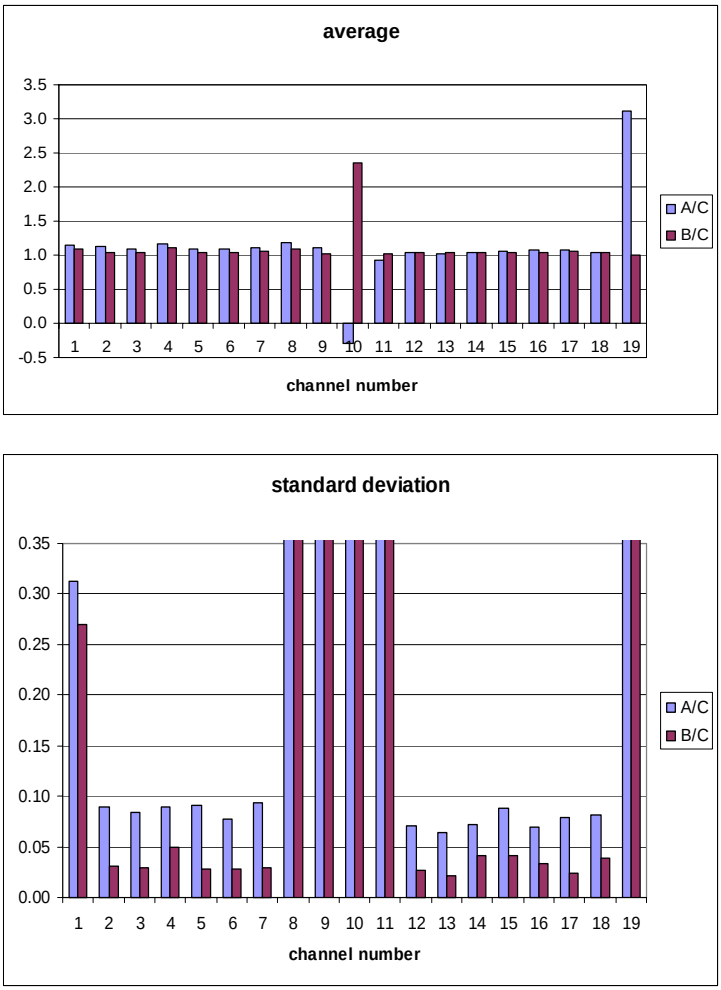

Fig. 3.4: Average and standard deviation for channel 1 to 19 when normalizing with calibration method C.

be expected. One way to get rid of this major disturbance is to divide the standard deviation with the average value. This has been done in figure 3.3. This graph shows a more flat behavior. But there is still some kind of disturbance remaining. Now showing up as a weak u-shape. It is also impossible to notice any remarkable or consistent correlation between the three cases. The u-shape however is due to the variations in the plasma emissivity profile. It tells us that the relative statistical scatter is less in the plasma center compared to the periphery, if the neutron emissivity profile is taken into account.

An alternative approach is to normalize the values for two of the calibration methods with respect to the values from the third one. The downside is that one is only

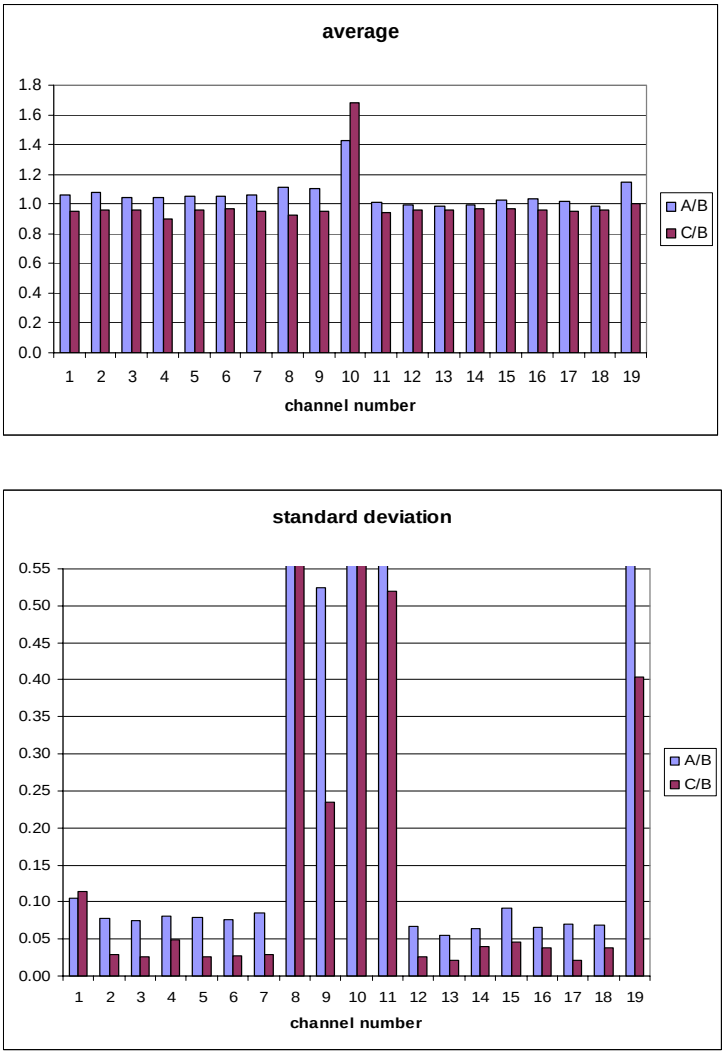

Fig. 3.5: Average and standard deviation for channel 1 to 19 when normalizing with calibration method B.

able to compare two methods at a time. To start with, the results of method C were used as reference for the reason that this method is expected to be the most accurate one. The results are presented in figure 3.4. These indicate that the average is rather constant through the channels for both methods with the notable of channels 10 and 19. The same trend is found for the standard deviation but now there are more break-away channels (1, 8-11 and 19). There is also a greater difference between the results of methods A and B, where those of B are systematically lower. The observation that the peripheral channels (1, 10, 11 and 19) deviate could be a matter of statistics which could also affect the results for channels 8 and 9. What is significant, though, is the systematically lower values for the standard deviation for method B, which suggest that this is the more reliable one of the two methods. If method B is used as reference, one obtains results that are similar to these above (figure 3.5). This would indicate that method B and C work about equally well for calibration purposes.

3.2 Time integrated data

At the first sight one may intuitively think that there would not be any significant difference between the time-resolved and time-integrated data. However, as shown below, this is not the case. Using time-integrated data has both advantages and drawbacks. The advantage is that one can expect a greater number of neutrons per channel than in the time-resolved case, leading to less statistical scatter. On the other hand, the data set will consist of fewer but larger samples, i.e. only one per discharge. The results (figure 3.6) are quite similar to those of the time-resolved case with respect to averages. The standard deviation results, however, differ from those of time-resolved case. As expected, the larger size of the data samples causes increased statistical scatter among the samples. So the overall standard deviation increases. Also due to the large sample size the statistical scattering within a specific channel will be reduced. So the calibration effects show up more strongly and a rise of the standard deviation for the A-method can be observed. This becomes even clearer if the neutron yield distribution effect is eliminated through calculating the standard deviation to average ratio as it was

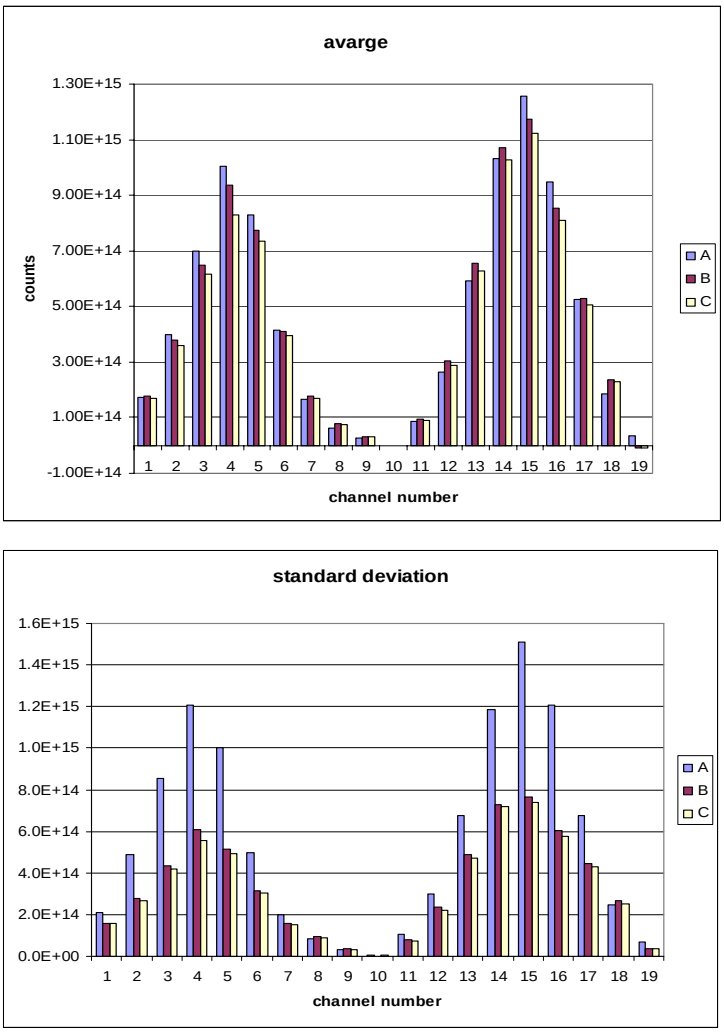

Fig. 3.6: Average and standard deviation graphs for time-integrated data.

in the time-resolved case. This is illustrated in figure 3.7. This graph indicates that calibration method A is less accurate than method B and C but there is still nothing to suggest a difference between B and C. This is in agreement with the result from the time-resolved case.

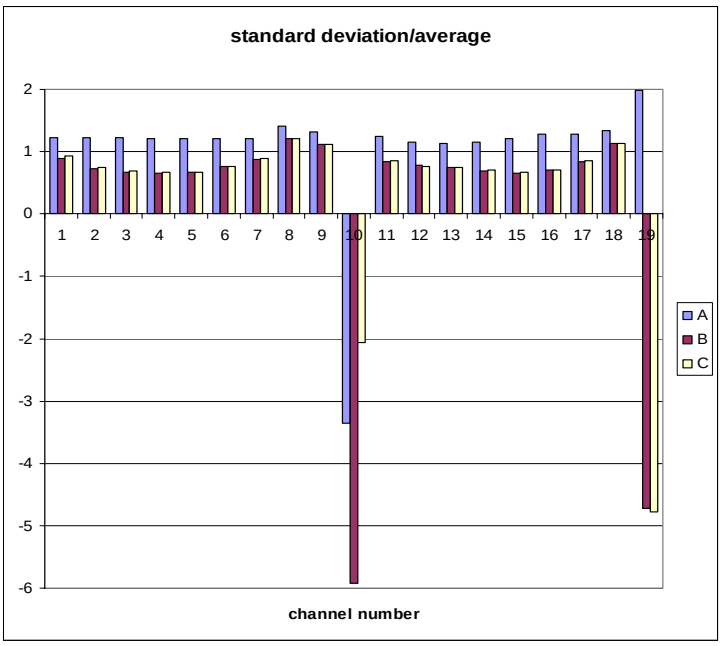

Fig. 3.7: Standard deviation divided with the average value for channel 1 to 19 for time-integrated data.

3.3 KN3/KN1 ratio VS total neutron yield

It is of interest to analyze how the KN3/KN1 ratio varies with the total neutron yield (Y_n). Unfortunately, the amount of integrated data is not sufficient to perform a detailed analysis but some information can be obtained from the time-resolved data, for the study of contour plots of KN3/KN1 vs Y_n in a rather coarse grid system (20x40). The results are shown in figure 3.8. It appears that the scatter in KN3/KN1 ratio increases with decreasing total neutron yield. This is true for all the three calibration methods. As the total neutron yield increases, the KN3/KN1 ratio approaches a value close to 1. The average values are 1.090, 1.045 and 0.997 for method A, B and C respectively. Further inspection of the C graph shows that almost all points in the cluster gathered around the coordinates ($2.2*10^{14}$, 1.1) in figure 3.8 c) originate from shot number #53313. This indicates that applying calibration method C to KN3 data from this specific shot did not worked out properly. If discharge #53313 is excluded the average KN3/KN1 ratio for method C adopts the value 0.994 which still is the one closest to 1. This implies that method C is the most accurate and that method A is the least accurate. The result supports what has already been noticed and shows an even clearer separation between B and C.

This is further strengthened by the results on the standard deviations of the KN3/KN1 ratios, which take the values 0.052, 0.035 and 0.033 (again discharge #53313 was excluded) for method A, B and C respectively.

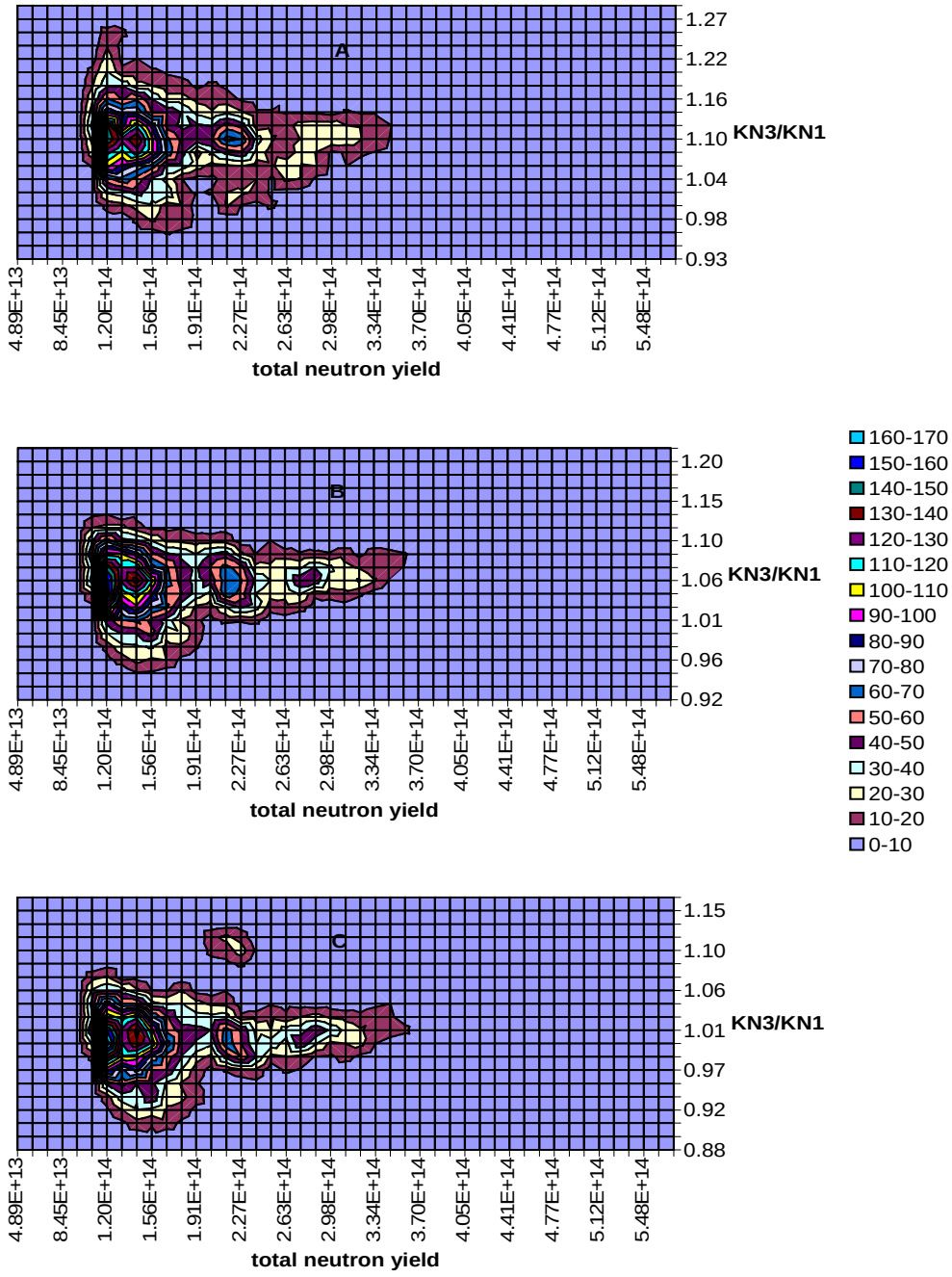

Fig. 3.8: Frequency contour plots showing the KN3/KN1 ratio vs the total neutron yield.

4. Calibration changes and discriminator/gain drifts

Figure 4.1 shows a sample of a pulse height spectrum for KN3 reflecting the response to the neutron emission from a D plasma. The spectrum is recorded by one of the central channels in the horizontal camera using the liquid scintillator detector. The low energy rise starting at around channel #60 is due to the 2.45-MeV neutrons with a cut-off by the discriminator at about channel #27 (indicated) which is set correspond to a proton energy of $E_{thres} \approx 1.8$ MeV. Because of the finite energy resolution, the discriminator shows a smoothed cut-off. The small peak on the right hand side (near channel #200) is a pulser signal that artificially gets compressed in the ADC

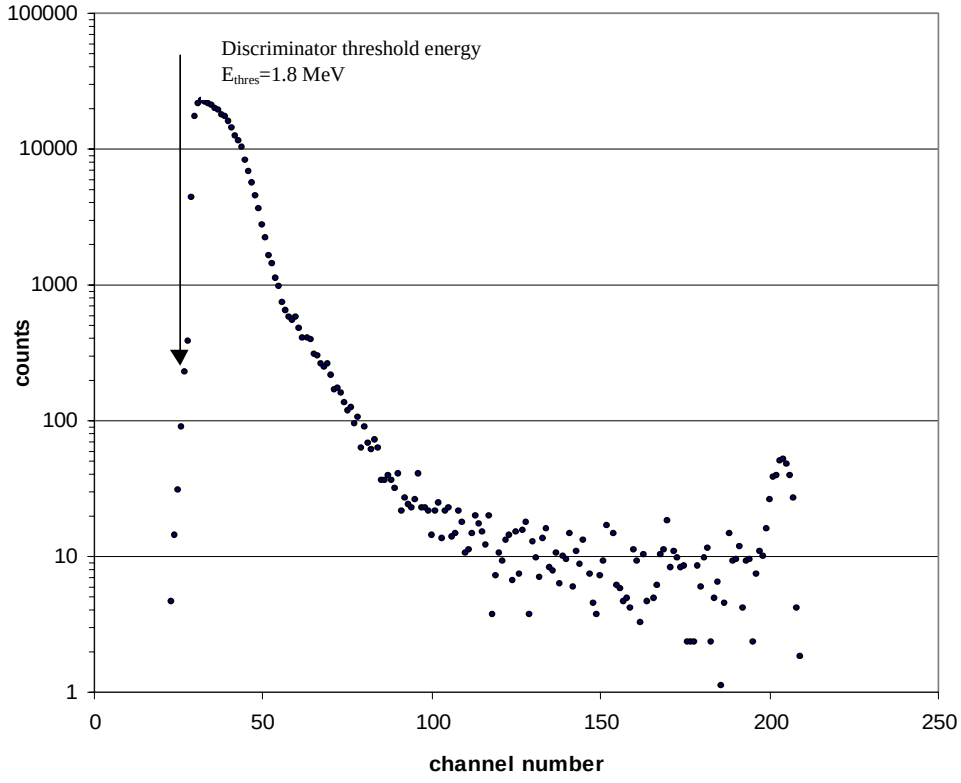

Fig. 4.1: Pulse height spectrum recorded by the NE-213 detector in channel 4 for a random shot. The spectrum has been dead-time corrected. The edge on the left-hand side is the discriminator threshold cut-off, set to $E_{thres} \approx 1.8$ MeV.

(Analogue-Digital Converter) recording. There is also a contribution from the 14-MeV neutrons of low intensity showing up in the region between channel number #100 and #190. This interval may also contain some contributions from high-energy γ-rays. The cause of the slope ranging from channel #60 to #100 is unclear. However, this is the range where pile-up effects would show up as well as pulses caused by γ-rays and neutrons produced in fast ion reactions such as $^{9}Be(d,n)^{10}B$ [10]; the latter reaction occur when plasma deutrons are accelerated by the applied radio frequency heating and beryllium constitutes plasma impurity.

The typical discriminator setting corresponds to a total efficiency (η_{tot}) of about 4 % for detection of 2.5-MeV neutrons from $d + d \rightarrow {}^{3}He + n$ reactions. The pertinent question is therefore what will happen if the threshold would drift a few percent in either way. As shown in figure 4.1, the threshold energy is in a region with a very steep gradient. This implies that small fluctuations in the threshold level could cause rather dramatic changes in the detector efficiency. In order to assess the drift sensitivity of the neutron detection efficiency, one also has to consider the relative background rejection efficiency of the detector. This is done below.

4.1 Estimation model

The energy distribution of the recoil protons induced by 2.5-MeV neutrons is constant up to a maximum value of E_p=2.5 MeV. When measured with a detector of finite energy resolution, the 2.5-MeV limit of this box distribution will be smoothened and causing a progressive rise with decreasing energy. This is due to the non-linear relationship between pulse-height response and energy. To this end, a theoretical response spectrum was calculated, consisting of two convoluted parts, the rectangular recoil energy distribution (R), a Gaussian (G) to represent the finite energy resolution and the light-yield function (L_p). The functions s and g were convoluted into a new function, using the relation

$$\frac{dN}{dE} = \int G(E, E') * R(E') dE' \qquad (4.1)$$

where dN/dE is the pulse height as a function of proton energy (E_p). G has a relative energy resolution of 20 % (FWHM) which is a reasonable assumption for this kind of application; R ranges from 0 to 2.45 MeV and the height is set to 0.4 in order to attain unity (i.e., the integral over the curve equal to 1) for normalization aspects. Moreover, the pulse height can be expressed as a function of light output using the relationship

$$\frac{dN}{dL_p} = \frac{dN}{dE} / \frac{dL_p}{dE} \tag{4.2}$$

The light output function in equation (2.2) is only valid in the range 1.5 to 3.3 MeV and has to be complemented to extend to lower energies. It is known that for many organic scintillators, the light output can be represented as proportional to $E^{3/2}$, for energies below 5 MeV [11]. It was shown that $L_p(E)=0.19E^{3/2}$ was in good agreement to equation (2.2) in the range between 1.5 and 3.3 MeV and was therefore adopted as an approximation. The resulting pulse height spectrum is shown in figure 4.2. It is known that the threshold energy in the considered case is $E_{thres}\approx 1.8$ MeV and the maximum proton recoil energy is $E_p=2.45$ MeV. Hence the corresponding light outputs, $L_p(1.8)$ and $L_p(2.45)$ can be calculated. One can now derive the nominal efficiency value (η_0), which is, the fraction of the recoil protons that have a kinetic energy exceeding the threshold level (corresponding to $L_p\approx 0.45$ in figure 4.2). This value works as a reference point, which is compared to the actual efficiency values that can vary due to a threshold change. The efficiency change can be derived from the expression

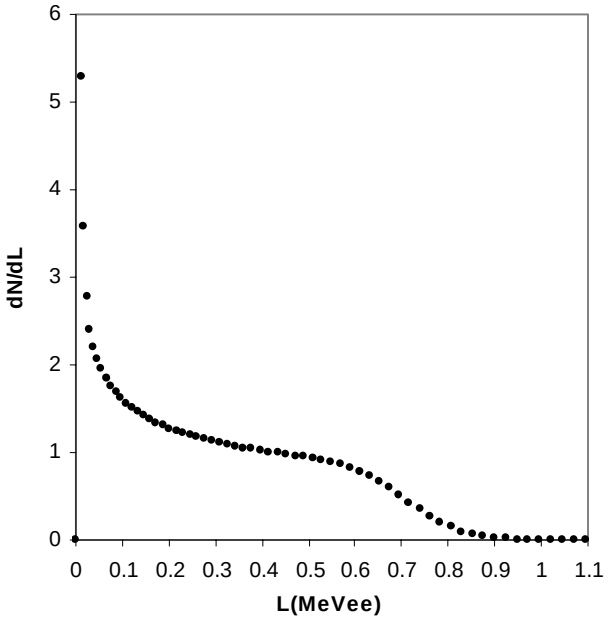

Fig. 4.2: Theoretical pulse height spectrum with an energy resolution of 20 %.

$$\frac{\Delta\eta}{\eta_0} = 1 - \frac{\eta}{\eta_0} \tag{4.3}$$

where $\eta=\eta(E_{thres})$ is the new efficiency. The drift in threshold energy is represented in terms of changes in gain (G), i.e., $1-\eta_0$. Calculations have been performed for changes of $\Delta G/G=1$, 3 and 5 %.

The total efficiency (η_{tot}) is the product of the intrinsic efficiency, η_i taken as the ratio between registered and "impinging" detector events and the geometric efficiency, η_{geom} taken as the fraction of the source radiation which is geometrically intercepted by the detector.

$$\eta_{tot} = \eta_i \eta_{geom}. \qquad (4.4)$$

Moreover, η_i can be subdivided into two parts, reflecting the physical properties of the detector and the discriminator there we shall consider the discriminator (and gain) dependent factor of the efficiency.

4.2 Calculations

In the calculations below we have only considered the case where the discriminator drifts to the right, i.e., threshold energy increase. The case where the discriminator drifts to the left should give similar results for such small drifts as in this case.

The initial fraction of recoil protons whose kinetic energy exceeds the threshold energy, E_{thres}=1.8 MeV is

$$\eta_0 = \frac{\int_{1.8}^{2.45} dN}{\int_{0}^{2.45} dN} \approx \frac{11.3}{103.1} \approx 10.9\%$$

Table 4.1 shows the calculated results in terms of absolute and fractional η-values for gain changes of 1, 3 and 5 %. It can be seen that even small discriminator/gain changes result in comparatively large changes in efficiency. The relationship between $\Delta G/G$ and $\Delta\eta/\eta_0$ is approximately linear with a ratio of about 1:8. This shows why the discriminator/gain stability is such an important issue for neutron camera measurements and the need for its close monitoring. The stability issue will be even more highlighted for long pulse operation modes, such as for the ITER case.

Table 4.1: Calculated efficiency values for different levels of the threshold energy; ΔG/G=1, 3 and 5 %.

ΔG/G [%]	Δη [unit %]	$\Delta\eta/\eta_0$ [%]
1	0.89	8.2
3	2.67	24.5
5	4.45	40.8

5. Comparison of JET experience and ITER plans

When the next step nuclear fusion device, ITER, with a planned power production in the GW-range becomes reality, reliable and accurate diagnostic systems will be even more important than it is today. It is, and has been so for several years, a common thought that a neutron profile monitor would contribute to essential information in the operation of such a large-scale fusion device. This derives from on the experience of neutron cameras gained at present fusion research plants such as JET and TFTR (Tokamak Fusion Test Reactor). The main functions of a neutron camera on ITER would be to give information about the total neutron yield rate (Y_n) and the 2-D neutron emissivity distribution; i.e., the same abilities that are significant for the neutron camera at JET. However, to this should be added another feature, namely, to provide input for the feedback control system. The feedback control system will be impartial for the operation of ITER, where discharges with duration up to a thousand seconds have to be monitored. Clearly, there will be many strict requirements on keeping the neutron camera detector system stable under these operating conditions. Moreover, there will also be demands on the sight-lines through the plasma which is the issue we consider next.

The need for straight line-of-sights penetrating the machine structure makes the interface difficult. Recently ITER has been redesigned in order to meet new objectives and cost constraints, implying that the machine structure has become more compact and

thus allowing less space for the diagnostic systems. The new design, ITER-FEAT, has brought significant interface restrictions for implementing a neutron camera. As an example these involve a reduced vertical aperture for the horizontal camera.

5.1 The evolution of neutron cameras for ITER

Over time, a number of different neutron camera facilities for ITER have been considered. To show the variation among the techniques suggested we can mention, flowing water activation loops (L.C. Johnson, et al., 1998), magnetic proton recoil technique (J. Källne, G. Gorini, 1991) and recoil proton counter-telescope technique (T. Nishitani, et al., 1996), can be mentioned. However, neutron cameras with fanlike geometry (similar to the neutron profile monitor at JET and TFTR), are those considered to be the most appropriate. The main issue is to optimize the number of lines-of-sight, involving aspects such as plasma coverage, smoothness in implementation etc. The ideal case would be to have two (one horizontal and one vertical) fan-shaped collimator arrays, with a large number of collimators in order to cover the whole plasma and to attain a good spatial resolution. However, because of other requirements, this ideal case will be restricted.

The latest version is a neutron monitor consisting of two cameras, one horizontal (12 channels) and one vertical (15 channels). The horizontal camera similar to the horizontal camera at JET but, due to the limited space, adjacent modules are slightly offset in the assembly of all the collimators. There are three juxtaposed vertical stacks of modules, tilted one degree in relation to each other, with four collimators in each. This allows a good spatial resolution, $\Delta r/a$ (~9 %, which is slightly better than at JET) even though the space is limited. The present design does not allow a single fan-like vertical camera. Instead the vertical camera system is obtained by distributing the fifteen channels in toroidally displaced poloidal planes (spatial resolution about 7 % in plasma center). The design is proposed by JCT (Joint Central Team) and is presented in the appendix at the end of this thesis.

Moreover it is envisaged that the same kind of detector assemblies as those used at JET will be used on ITER-FEAT. Hence, the experience gained at JET is a very useful source of information regarding this objective.

5.2 Neutron emissivity distribution

The poloidal neutron emissivity has a distribution (S) given by (JA HT report)

$$S(R,z) = \left[1 - \left\{\frac{(R - R_0 + \delta a - f(z))^2}{a^2} + \frac{(z - z_0)^2}{a^2 k^2}\right\}\right]^m \qquad (5.1)$$

where

$$f(z) = \delta a\left[1 - \frac{(z - z_0)^2}{a^2 k^2}\right]^n \qquad (5.2)$$

The parameters in equation (5.1) and (5.2) are described in table 5.1. The values shown in the table are reference values for D-T plasma operation in the present design of ITER. Figure 5.1 shows a plot of the neutron emissivity distribution with the parameter setting in table 5.1. It is assumed that the neutron source (i.e., the plasma) is toroidally symmetric with 14-MeV neutron emission.

Table 5.1: Reference values of some basic machine and operation parameters for ITER.

Parameter	Unit	Value
Major radius, R_0	m	6.2
Minor radius, a	m	2.0
Triangularity, δ		0.33
Plasma center (vertical), z_0	m	0.53
Ellipticity, k		1.7
Power of parabolic profile, m		0.8
Strength of triangular shape, n		0.5

The line-integrated neutron emissivities of the plasma gives the brightness distribution, B_λ (for sight-lines λ) seen by the neutron cameras from which, for instance, Y_n can be determined. This requires that the plasma coverage is sufficiently large. The

B_λ-distribution has been calculated using the approximation of representing the iso-emissivity with concentric ellipses. A random error of 5 % was applied to the calculations. The parameter values used are the same as in table 5.1 but without any triangularity. The results for the vertical and the horizontal cameras are illustrated in figure 5.2 (a) and (b) respectively. As the B_λ-distribution of the horizontal camera is

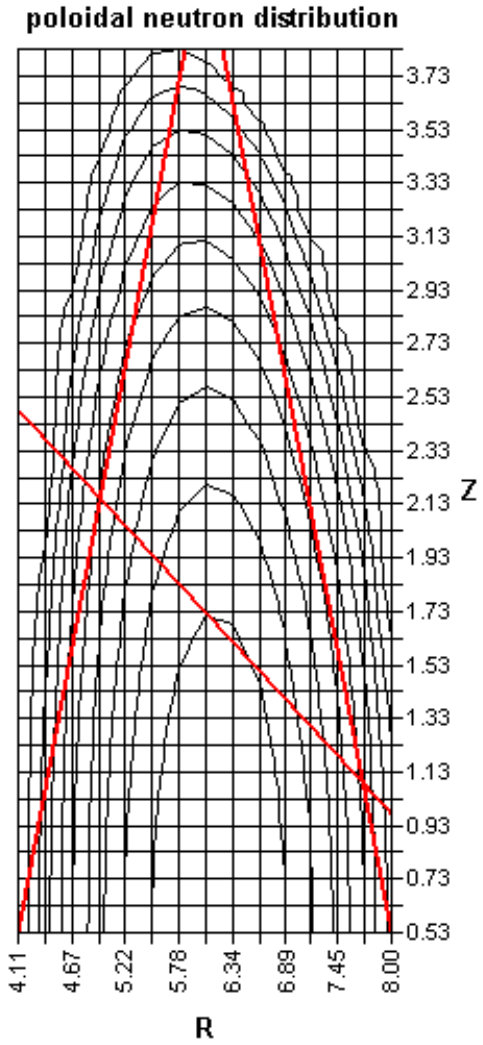

Fig. 5.1: Poloidal plane (upper half) contour plot of calculated iso-emissivities for an ITER D-T plasma based on the plasma conditions described in the text. The red straight lines illustrate the peripheral lines-of sight of the proposed vertical and horizontal neutron cameras for ITER.

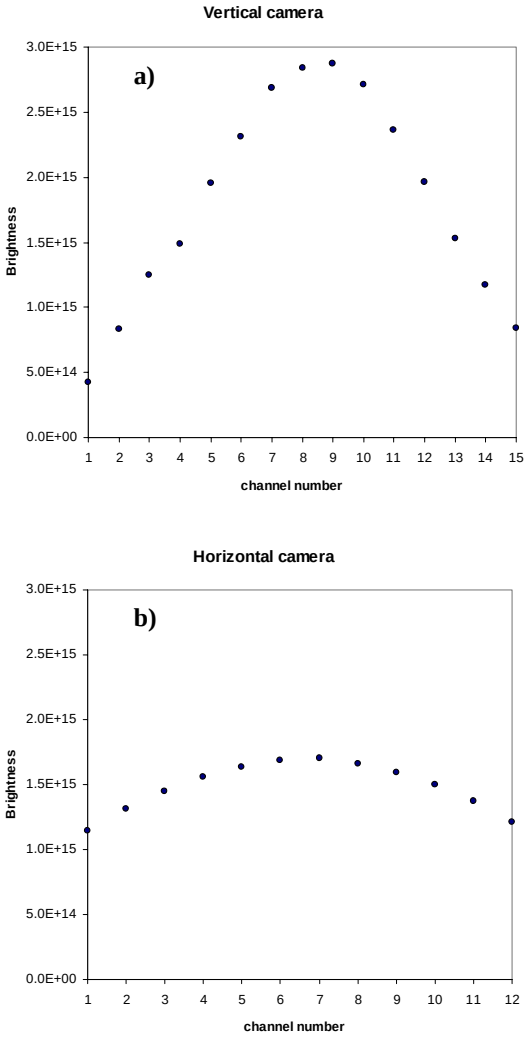

Fig. 5.2: Brightness distributions of the vertical (a) and horizontal (b) neutron cameras for ITER, assuming a pure elliptical iso-emissivity and a peaking factor of α=1.8.

rather flat covering only the upper 35 %, the Y_n determination would be very uncertain. Therefore, additional information from the vertical camera is essential.

5.3 Interface restrictions

It is clear from the peripheral lines-of-sight shown in figure 5.1 that the plasma height coverage is far from satisfying. The vertical camera has a plasma coverage that can be estimated to about 50 %, on the plasma axis. In comparison, the corresponding value for the neutron camera at JET is about 75 % [15]. The restricted coverage of the ITER cameras will play a significant role in cases when the plasma neutron emissivity is flat, i.e., for low peaking factor values. The relation between α and m is $\alpha = m+1$, so the emissivity in figure 5.1 has α=1.8, which corresponds to a very flat distribution indeed.

As the vertical detector channels looks into the plasma at different poloidal sections it requires that the toroidal emissivity distribution is isotropic in order to deduce a homogeneous poloidal emissivity profile. In the ignited phase, without auxiliary heating, the plasma neutron emission is isotropic and toroidally symmetric, so the vertical camera should be appropriate to deduce an emissivity profile. Moreover, nothing in the experience from the operations at JET implies any signs of anisotropic effects. Because of the similarities, both geometrically and operational, of JET and ITER there would probably be no toroidal anisotropy at ITER.

Because of the severe problems that comes with the interface of the vertical camera, calculations assuming reduced number of channels also has been performed. These showed that the ellipticity (k) and the radial centroid value (R_0) of the emissivity could be determined with reasonable accuracy even though only channels 3, 8 and 13 were used. For this case the errors turn out to be 6 % and 3 cm for k and R_0 respectively. The corresponding values when all fifteen channels were used are 3 % and 1 cm. However, if only the central channel 8 is used, the errors for both k and R_0 deteriorate markedly.

6. Conclusion and outlook

This thesis describes the neutron profile monitor (neutron camera) at JET. The neutron camera is one of the most important neutron diagnostics devices operating at JET. Its main capabilities are to measure the total neutron yield rate (Y_n) as well as the poloidal emissivity profile distribution. In particular, the calibration system is investigated. Comparison of the three different calibration methods, A, B and C, showed that method C is the most accurate one. This is also the method that is used today. However, the ^{22}Na γ-source used for the calibration purpose decay with a half-life of 2.6 years, which implies that one has to resort to other solutions in the future.

Another calibration issue relates to the stability of the discriminator threshold. It is reasonable to assume that the threshold level drifts back and forward, within a few percent over time. A qualitative sensitivity analysis showed that small fluctuations in gain (1-5 %) result in about eight times larger changes in efficiency. Effects of this kind are important to have in mind when working on a neutron profile monitor for ITER, where the stability issue is even more important due to the longer duration times. In this context, future studies of the neutron camera at JET will play an important role, as it is envisaged that the detectors would be of the same kind at ITER.

The present design of ITER-FEAT does not allow an optimal interface of neutron profile monitors. Limitation in space brings some interface restrictions. The plasma coverage of the horizontal camera is one of the most affected features. For strongly peaked neutron emissivity profiles this will play a less important role. A good spatial resolution can be achieved if the channels for the vertical camera are distributed toroidally and the adjacent channels for the horizontal camera are slightly offset. Recently some calculations of the neutron iso-emissivity distribution and the brightness distribution have been performed that have give brief information about the plasma neutrons under ITER conditions. However, to get the whole picture more detailed calculations, similar to the MCNP calculations that preceded the construction of JET, has to be done.

Acknowledgements

This diploma work has become reality thanks to several people. First of all I would like to thank my supervisor Professor Jan Källne who is the one that introduced me to the exciting field of fusion research. Jan has support me during the whole time I have been working on this diploma thesis and his experience have been a great source of information and inspiration. During the introducing week at JET, Hans' knowledge about how things work at JET was invaluable. Hans helped me to find a way out of the administrative "jungle" and he has always been available to answer all my questions. Well at JET I have Sean to thank for his involvement in my work. Thank You for showing patience and supporting me with the data I needed for my work. Göran and Anders shared the second trip to JET with me; even though it was short, it was fruitful and enjoyable. You two also have shared many battles on the floorball court with me, which has been great fun! Of course Göran and Anders also have helping me out in all kind of tricky situations that have appeared during my work. My friends and former classmates David and Elsa who started their diploma work a few months earlier than I at INF have encourage me and have contributed to raise the social factor during my period at INF several levels. I would like to thank You both by wish You good luck with all Your future doings! I also like to thank my diploma worker colleague and Italian friend Luca. Thanks for always being in such a good mood and for letting me stay at Your place in Milan after the Varenna conference! My gratitude also goes to everyone at INF.

Finally, I would like to show my gratefulness to my family by dedicating this thesis to them; thank You for showing Your interest and support during all my studies in Uppsala. Special thanks to my Father, for exploring the pubs in Oxford with me; it would not have been as much fun without You!

References

[1] M. Stanley Jr., *Fusion*, Weston, 1984.

[2] J. Wesson, *The science of JET*, JET joint undertaking, Abingdon, Oxfordshire, 2000.

[3] EFDA-JET website, URL; http://www.jet.efda.org, 2001.

[4] ITER homepage, URL; http://www.iter.org, 2001.

[5] *Annual report 1999*, JET joint undertaking, Abingdon, Oxfordshire, 2000.

[6] P. Prandoni, *The MPR spectrometer for fusion neutrons*, Uppsala University Neutron physics report, UU-NF 98 #1, 1998.

[7] O N. Jarvis, Neutron diagnostics, JET, Culham Science Centre, private communications, April 2001.

[8] G J. Sadler et al., *Calibration issues for neutron diagnostics*, JET joint undertaking, Abingdon, Oxfordshire, 1997.

[9] J M. Adams, O N. Jarvis, G J. Sadler, D B. Syme, N. Watkins, *The JET neutron emission profile monitor*, JET joint undertaking preprint JET-P(92)27, 1992.

[10] S. Conroy, Neutron diagnostics, JET, Culham Science Center, private communications, April 2001.

[11] G F. Knoll, *Radiation detection and measurement*, third ed., Wiley, 2000.

[12] K S. Krane, *Introductory nuclear physics*, Wiley, 1988.

[13] S. Conroy, *YAPAN documentation*, Abingdon, Oxfordshire, 1999.

[14] S. Conroy, Neutron diagnostics, JET, Culham Science Center, private communications, Fortran code, February 2001.

[15] F B. Marcus, et al., *A neutron camera for ITER (invited)*, American Institute of Physics, 1997.

Appendix- JCT proposal

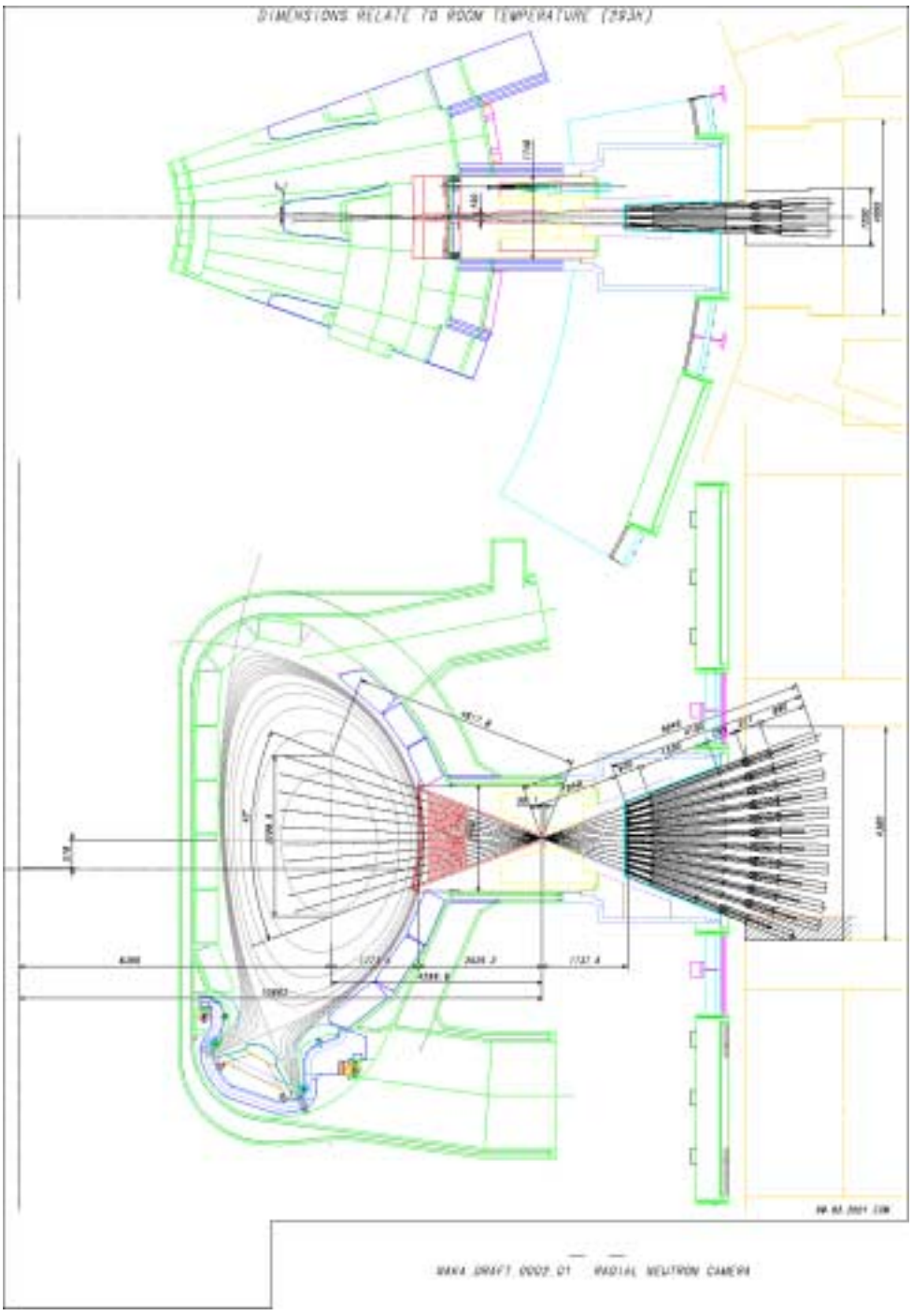

Fig. A1: Radial neutron camera seen from above and from the view of the poloidal cross section.

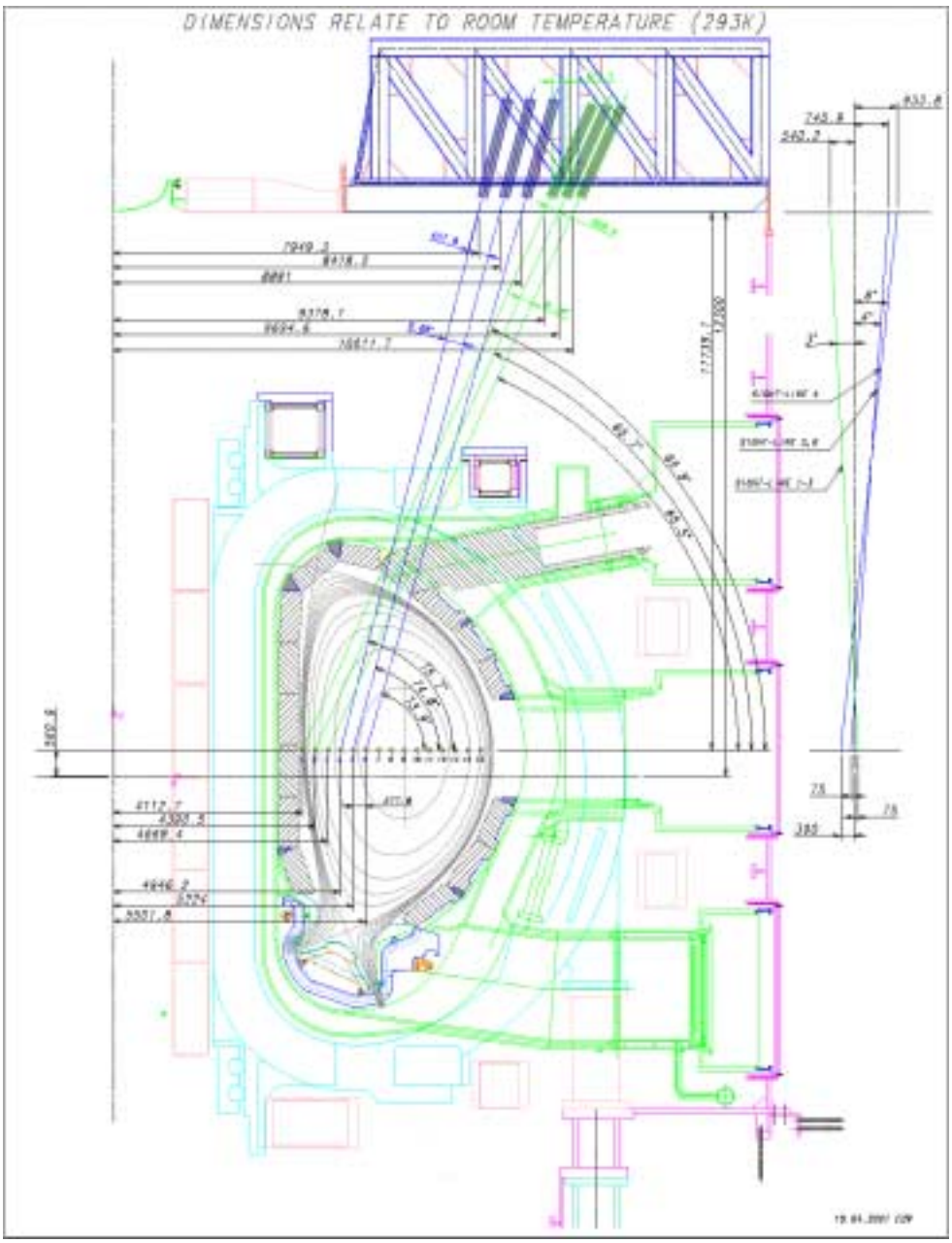

Fig. A2: Vertical neutron camera, sight-line 1 to 6.

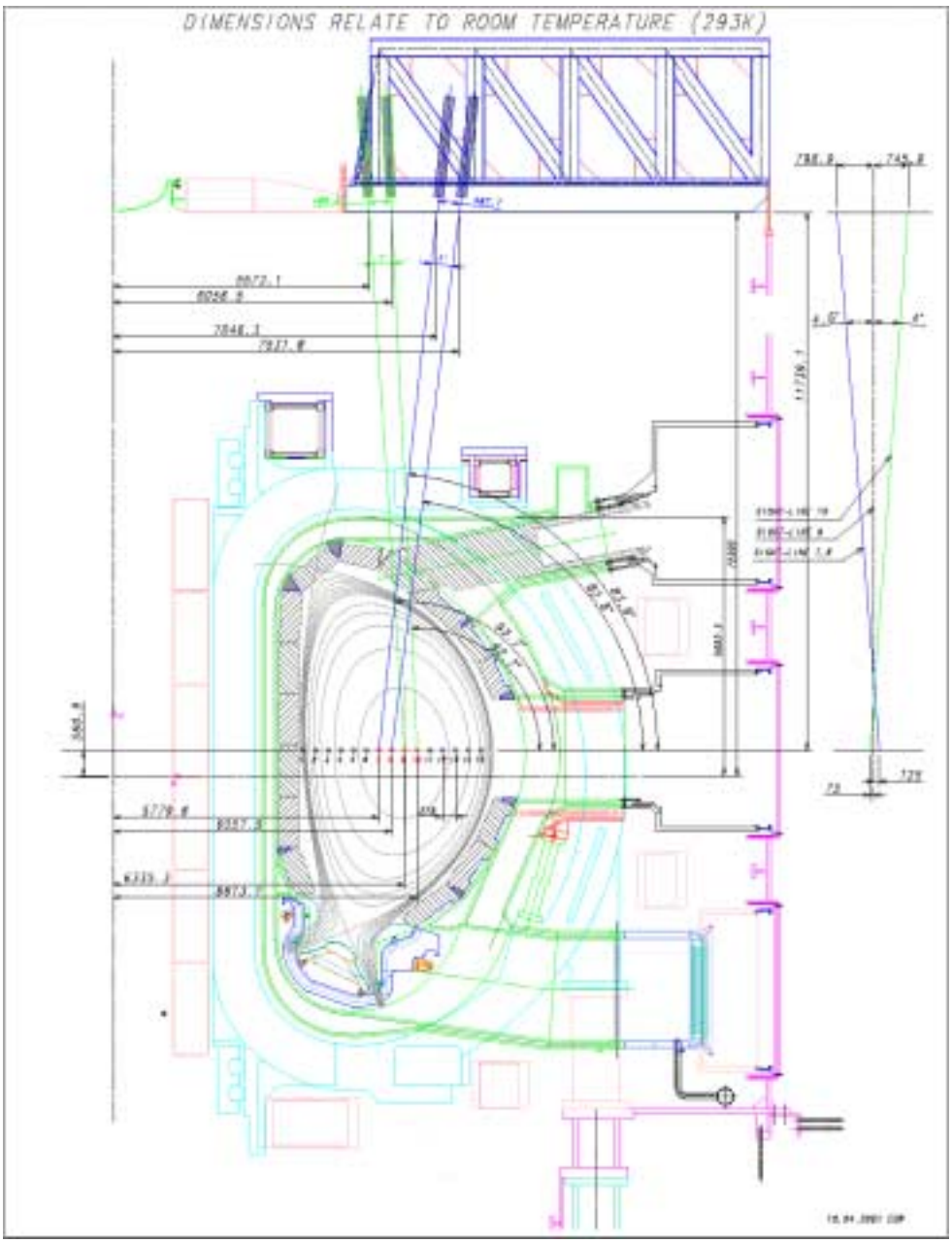

Fig. A3: Vertical neutron camera, sight-line 7 to 10.

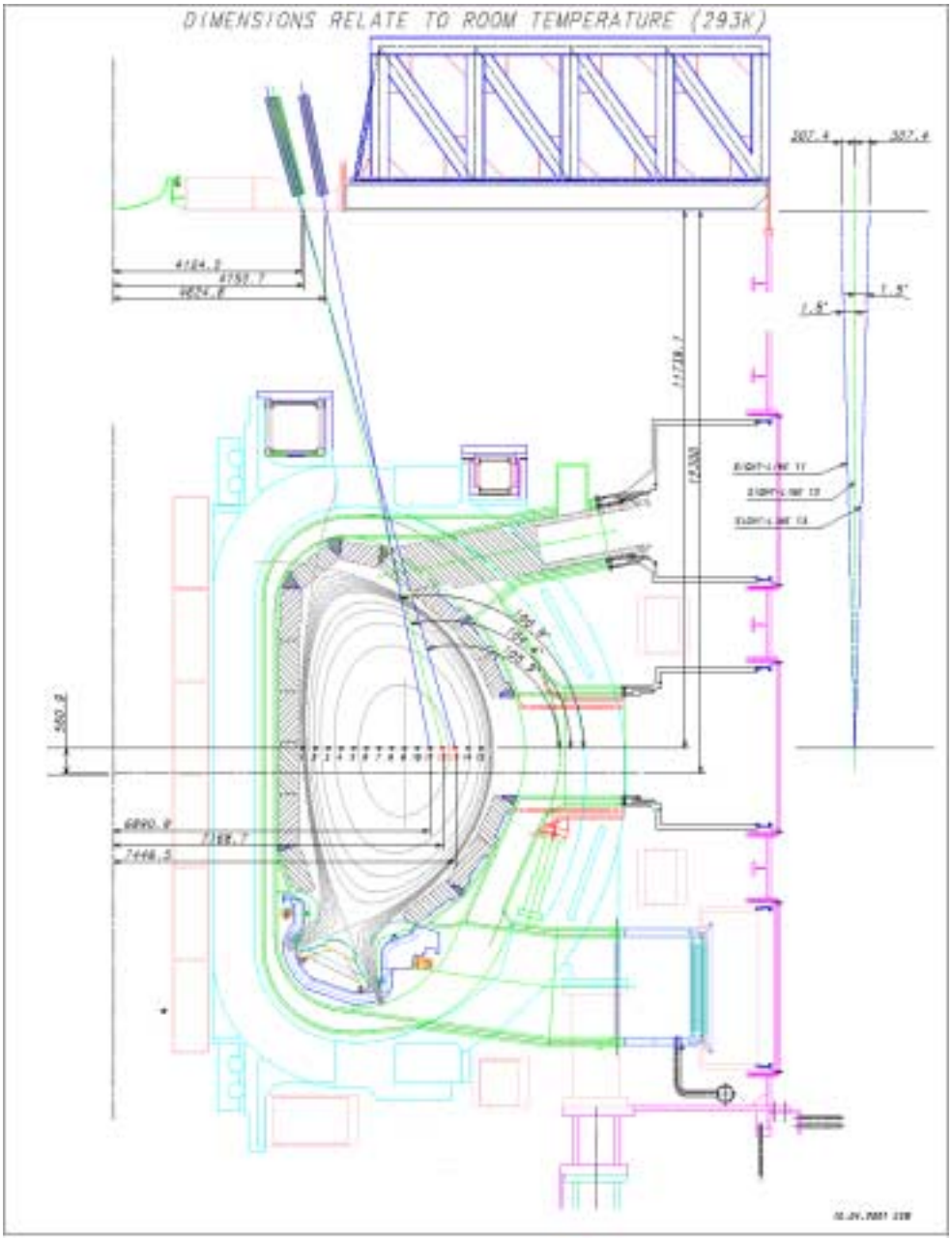

Fig. A4: Vertical neutron camera, sight-line 11 to 13.

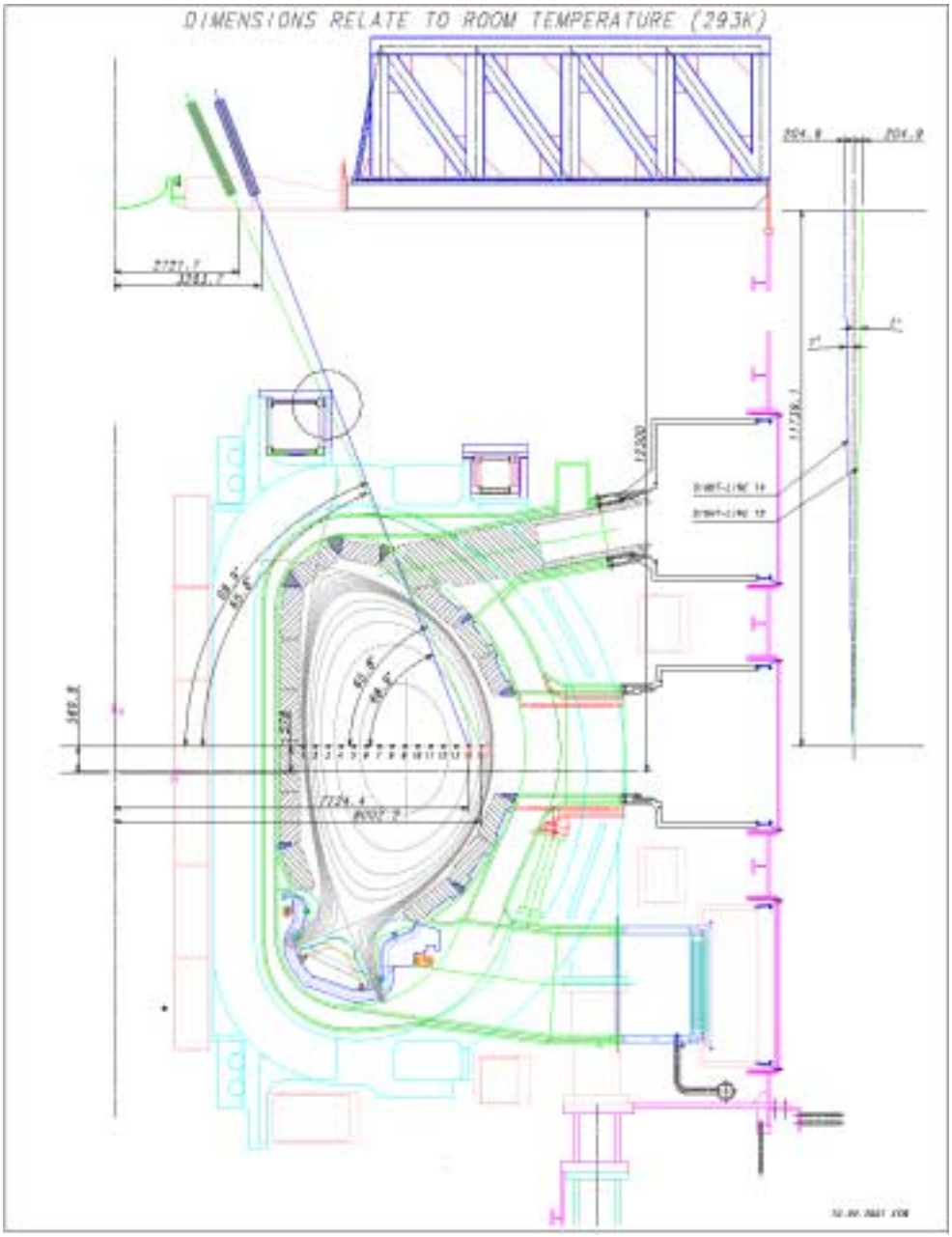

Fig. A5: Vertical neutron camera, sight-line 14 and 15.